

Received February 18, 2020, accepted March 22, 2020, date of publication March 30, 2020, date of current version April 15, 2020.

Digital Object Identifier 10.1109/ACCESS.2020.2984246

# Integration of 5G Rectangular MIMO Antenna Array and GSM Antenna for Dual-Band Base Station Applications

YUFENG ZHU, YIKAI CHEN<sup>ID</sup>, (Senior Member, IEEE), AND SHIWEN YANG<sup>ID</sup>, (Fellow, IEEE)

Department of Microwave Engineering, University of Electronic Science and Technology of China, Chengdu 611731, China

Corresponding author: Yikai Chen (ykchen@uestc.edu.cn)

This work was supported by the Natural Science Foundation of China under Grant 61971096, Grant 61671127, Grant 61631006, and Grant 61721001.

**ABSTRACT** In this paper, a dual-band dual-polarized antenna array is presented for 5G base station application. The developed antenna array consists of a  $4 \times 4$  planar MIMO array operating at 3.3-5.0 GHz band (upper band UB) and a single antenna element working at 0.69-0.96 GHz band (lower band LB). The dual-band operation is based on our previously proposed antenna topology. The novelty of this paper is that the UB antenna array is a large-scale rectangular lattice array with 16 antenna elements for practical MIMO applications. Meanwhile, both the cross-band and in-band mutual coupling among the LB and UB antennas are furtherly suppressed by employing three decoupling techniques including rectangular ring resonator, ferrite chock ring, and novel baffle structure. With these decoupling technologies, the UB antenna array and the LB antenna are successfully integrated within a compact volume of  $0.93\lambda_L \times 0.93\lambda_L \times 0.17\lambda_L$  ( $\lambda_L$  is the wavelength at 0.82 GHz). Experimental results show that the proposed dual-band antenna array offers high cross-band port isolation ( $> 30$  dB). Stable radiation patterns are also achieved for both the LB and UB antennas with averaged gain of 8.6 dBi and 7.3 dBi, respectively. The radiation efficiency is higher than 90% across the entire operation bands. It is the first time to realize a large scale sub-6 GHz MIMO antenna array shared-aperture working with a GSM band antenna element in a such compact volume.

**INDEX TERMS** Dual-band antenna, base station antenna, compact size antenna.

## I. INTRODUCTION

The upcoming fifth generation (5G) communication era will be an important step forward in wireless communication system evolution. To enhance the throughput of wireless systems and be able to support a large number of users, massive MIMO (Multiple-Input Multiple-Output) antenna configuration has been a significant technology in 5G antenna system [1]–[5]. However, the new operation band and the large number of antennas require additional installation volume, which inevitably aggravate the limited radiation aperture over base station tower. It is expected that the sub-6 GHz massive-MIMO antenna arrays could be installed in the radiation aperture of the original 2G, 3G and 4G antennas.

Nowadays, researches mainly focus on integrating two linear antenna arrays operating in 2G/3G [6]–[9],

2G/3G/4G [10]–[14], and 4G/5G [15]. The embedded scheme is one of the most popular manufacturing technology in dual-band base station antenna developments. It benefits from simple structure and effective decoupling for higher and lower band antennas. However, it is limited by linear array configuration and the frequency ratio of the higher and the lower bands is requested to be around 2. Therefore, the embedded layout is hard to be applied in this work since the higher band antenna array is a planar antenna array and the frequency ratio between two bands is 5. To achieve dual-band planar antenna array configuration, multiband antenna element [16] and fragmenting dipole element [17] are proposed in the literature. However, the multiband antenna element could not maintain stable radiation patterns in higher frequency bands (i.e. 3.3-3.8 GHz). Meanwhile, the fragmenting dipole antenna suffers from insufficient working bandwidth to cover entire 0.69-0.96 GHz. To overcome this challenge, we propose to introduce a frequency selective

The associate editor coordinating the review of this manuscript and approving it for publication was Raheel M. Hashmi.

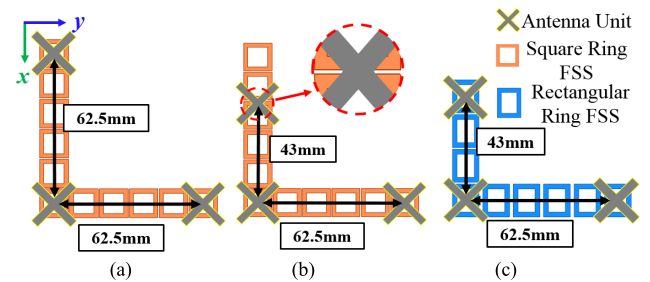
surface (FSS) in antenna array to realize dual-band, low-profile, and shared-aperture design [18]. In our proposed topology, upper band (UB) antenna array is placed above the FSS while lower band (LB) antenna is located under the FSS. Therefore, the proposed antenna layout is named as UB-FSS-LB topology. The FSS possesses nearly perfect reflective property in the UB and partly pass-band property in the LB. Accordingly, a  $2 \times 2$  planar UB antenna array was integrated with an LB antenna in [18].

However, the previous work merely focuses on validating the decoupling effect of the FSS. The UB antenna array in [18] is chosen to be small scale ( $2 \times 2$ ) to alleviate design difficulty. Moreover, large element spacing ( $0.68\lambda_U$ ,  $\lambda_U$  is the wavelength at 3.3 GHz) in the UB antenna array is set to avoid mutual coupling problem. It is obvious that such a simple UB antenna array could not be used as a massive-MIMO array in practice. Therefore, this paper presents a dual-band base station antenna design with large number of UB antennas covering 0.69-0.96 GHz and 3.3-5.0 GHz. The UB antenna array is extended from 4 elements to 16 elements while the elements spacing is reduced from  $0.68\lambda_U \times 0.68\lambda_U$  to  $0.47\lambda_U \times 0.68\lambda_U$ . The increased antenna elements and the decreased element spacing introduce three challenges compared to the primary work,

- i) The square-shaped unit cell of FSS will no longer be suitable to fill up the rectangular lattice of the UB antenna array;
- ii) There are 16 pairs of the coaxial cables of the UB antenna array intersected with the radiation aperture of the LB antenna. These coaxial cables will severely destroy the radiation performance of the LB antenna;
- iii) Mutual coupling in the UB array becomes unacceptable when element spacing decreases. It is necessary to introduce extra decoupling methods within the limited antenna space.

The aim of this paper is to address the challenges mentioned above and finally realize a large-scale dual-band base station antenna which has not been reported in the literature. To achieve this goal, three additional decoupling techniques are properly combined in this paper. Firstly, rectangular ring resonators are used in the FSS to adapt the rectangular configuration of the UB MIMO antenna array. Secondly, ferrite chock rings are introduced around coaxial cables to mitigate the induced currents which will destroy the radiation performance of the LB antenna. Thirdly, efficient decoupling baffle structures are designed to efficiently suppress the in-band mutual coupling in the UB antenna array. With these decoupling techniques, both the LB and UB antenna achieve satisfactory performance in a compact size of  $0.93\lambda_L \times 0.93\lambda_L \times 0.17\lambda_L$  ( $\lambda_L$  is the wavelength at 0.82 GHz).

The remainder of this paper is organized as follows. The applications and working principles of the three decoupling technologies are described in Section II. Simulated and measured results are presented in Section III. The comparison with other dual-band base station antennas is presented in Section IV. Section V concludes the paper.



**FIGURE 1.** Antenna array with various element spacing and FSS unit cell. (a) Square FSS with antenna element spacing of  $62.5 \text{ mm} \times 62.5 \text{ mm}$ ; (b) Square FSS with antenna element spacing of  $43 \text{ mm} \times 62.5 \text{ mm}$ ; (c) Rectangular FSS with antenna element spacing of  $43 \text{ mm} \times 62.5 \text{ mm}$ .

## II. THREE DECOUPLING TECHNIQUES

### A. APPLICATIONS OF THE FSS WITH RECTANGULAR RING UNIT CELLS

Fig. 1(a) shows the case in [18], in which the UB antennas are placed 62.5 mm away from each other in both  $x$  and  $y$  axis. As for a square lattice array, it is easy to design an FSS consisting of square ring resonators. An FSS composed by  $6 \times 6$  square unit cells with the length of 12.5 mm is able to cover one entire lattice of the array (only one column and one row of the FSS are shown in Fig. 1). As shown in Fig. 1(a), each UB antenna is located at the center of an FSS unit cell, the center area of the FSS unit cell without metallic coating is appropriate for feeding coaxial cables passing through. The outer conductor of the coaxial cable does not touch the metal part of the FSS, which guarantees stable frequency response of the FSS. Meanwhile, there is no need to solder the coaxial cable with the FSS, which eases fabrication procedure. However, to satisfy the beam scanning requirements, the antenna elements are usually arranged in a rectangular lattice instead of a square lattice. In this paper, the element spacing in  $x$  axis is reduced from 62.5 mm to 43 mm while the element spacing in  $y$  axis is kept as 62.5 mm. In such rectangular array configuration, the FSS consisting by square unit cells cannot ensure that each antenna element is located at the center of the FSS unit cell, as shown in Fig. 1(b). It is clear from Fig. 1(b) that some of the antenna elements locate above the gap between two adjacent square unit cells. In this case, the feeding cables of the UB antenna will touch the two adjacent FSS units, which destroys the frequency response of the original FSS. Therefore, as shown in Fig. 1(c), the rectangular ring resonator is required for fitting the rectangular array lattice and providing exactly the same electromagnetic (EM) environment for each UB antenna element.

In Fig. 2, an FSS with  $4 \times 6$  rectangular ring unit cells is designed to match one entire rectangular lattice of the UB antenna array ( $43 \text{ mm} \times 62.5 \text{ mm}$ ). The length of the rectangular ring unit cell is kept as 12.5 mm along the  $y$  axis. The length along the  $x$  axis is increased to 14.3 mm. However, as compared with FSS consisting of square unit cells, the rectangular FSS leads to different frequency responses in two orthogonal incident planes like  $xoz$  and  $yoze$  planes.

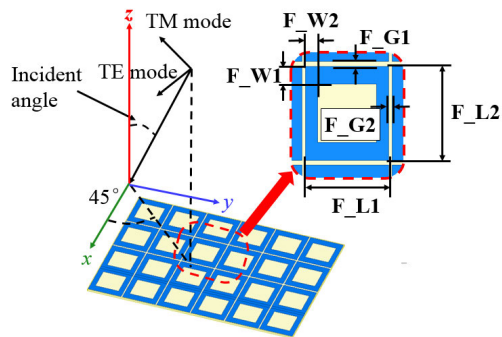


FIGURE 2. Configuration of the rectangular frequency selective surface.

It is well known that a square ring is equivalent to a parallel LC circuit in periodic boundary condition [19], [20]. The equivalent capacitance comes from the coupling between each ring through the gap while the equivalent inductance is produced by the currents flowing along the ring. Different lengths of the gaps along the  $x$  and  $y$  axis result in different equivalent capacitances. To compensate this effect, the equivalent inductance needs to be different along the  $x$  and  $y$  axis as well. The desired inductance's value is achieved by carefully designing the width of the rectangular ring. In the optimized unit cell, FW1 is slightly larger than FW2. The gap width  $F_{G1}$  and  $F_{G2}$  are tuned as well to further optimize the equivalent capacitance. The transmission characteristics of the rectangular FSS cell in periodic boundary conditions are presented in Fig. 3. According to the  $\pm 45^\circ$  polarization applications, the incident wave is restricted in the  $\varphi = 45^\circ$  plane. Due to the FSS is placed at the near field region of the UB antenna ( $0.2\lambda_U$  below the UB antenna), both the TE and TM waves should be considered to validate the reflection property of the FSS. As illustrated in Fig. 3(a), the FSS with rectangular ring resonators provides excellent reflection property for both TM and TE waves over the entire UB. With incident angle varied from  $0^\circ$  to  $45^\circ$ , the FSS still possesses transmission coefficients lower than  $-18$  dB. Most of UB EM wave will be reflected by the FSS. Therefore, the coupling between the UB antenna and LB antenna will be suppressed. It is suitable to replace the traditional perfectly electrical conducting ground plane with the FSS in the UB antenna array. Meanwhile, the transmission characteristics of the FSS in the LB are given in Fig. 3(b). The transmission coefficients range from  $-2.3$  dB to  $-8$  dB. This non-ideal pass band characteristic creates a new reflection path for the LB antenna. By carefully tuning the height of the LB antenna between the fixed FSS and ground plane, reflected waves from the FSS and the ground plane are out-of-phase at the LB antenna plane. Therefore, the two reflected waves cancel each other and a broadband impedance matching is achieved along with low-profile height and high gain characteristics. Detailed discussion on low-profile and broadband operation principle of the LB antenna can be found in [18]. This FSS is attractive for compact and low-profile height designs for 5G dense antenna arrays.

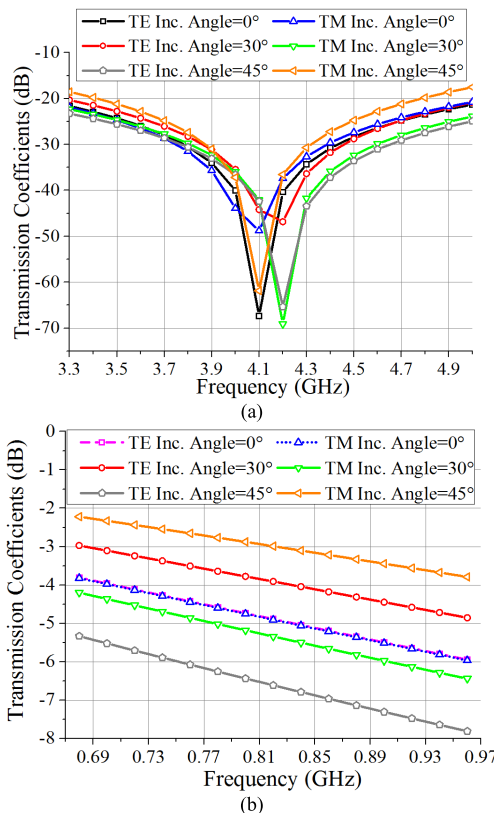
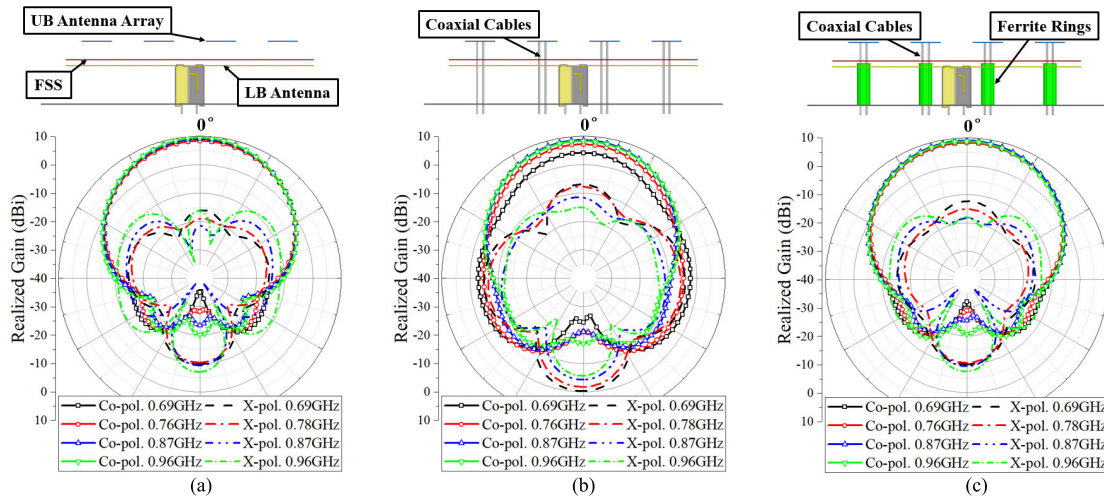


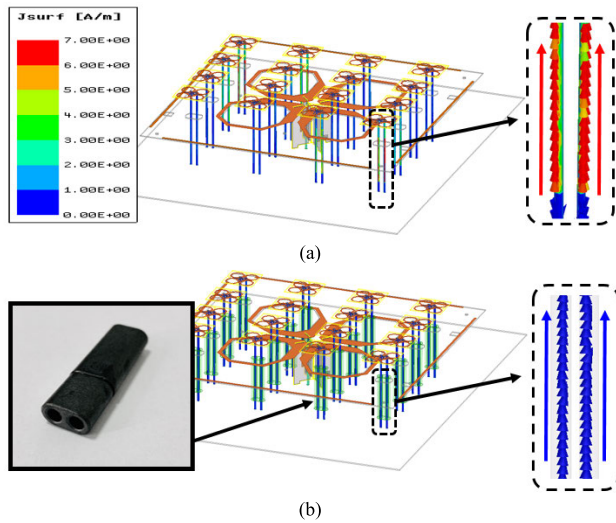
FIGURE 3. Transmission coefficients of rectangular ring FSS in (a) 3.3-5 GHz band and (b) 0.69-0.96 GHz band for different incident angles in  $\varphi = 45^\circ$  plane.

### B. APPLICATIONS OF THE FERRITE CHOCK RINGS

Another evitable problem in the UB-FSS-LB topology is that the coaxial cables of the UB antenna array will influence the performance of the LB antenna. Due to the stacked configuration of the antenna, the feeding coaxial cables of the UB antenna array intersect with the radiation aperture of the LB antenna. As for LB antenna, these coaxial cables can be seen as multiple metallic cylinders that touch the FSS layer and the ground plane. In previous work, only 4 pairs of the coaxial cables are concentrated at the center part of the LB antenna. The influence of these coaxial cables is negligible. However, when 16 pairs of the coaxial cables spread over the whole radiation aperture of the LB antenna, the EM environment for the LB antenna becomes complicated and limited. At some particular frequencies, part of radiation energy oscillates among these metallic cylinders. The oscillation deteriorates the impedance matching as well as the antenna gain of the LB antenna. For illustrative purpose, radiation patterns of the LB antenna with and without coaxial cables are shown in Fig. 4. From Fig. 4(a), the existence of the UB antennas do not affect the performance of the LB antenna because of their small electrical size. The LB antenna possesses a realized gain over than 8.5 dBi and a high cross-polarization discrimination (XPD) over than 25 dB. However, when coaxial cables are introduced around the LB antenna, there is an evident drop in



**FIGURE 4.** Simulated LB antenna radiation patterns in the antenna array (a) without coaxial cables (b) with coaxial cables and (c) with coaxial cables and ferrite choke rings.



**FIGURE 5.** Simulated current distributions on coaxial cables for cases (a) without ferrite choke rings; (b) with ferrite choke rings.

the gain of the LB antenna at 0.69 GHz. As shown in Fig 4(b), the gain decreases to 4 dBi and the XPD degenerates to 11 dB. The cross-polarization is also increased from  $-19$  dB to  $-7$  dB at 0.76 GHz. The deteriorations in base station antennas will lead to low signal reception quality of the whole communication system.

To suppress the parasitic coupling between the LB antenna and the coaxial cables, the induced currents on the outer conductor of the coaxial cables when the LB antenna is excited at 0.69 GHz are investigated in Fig 5(a). It clearly shows that strong induced currents flow on each pair of coaxial cable in the same direction with nearly equal magnitude. The induced currents produce secondary radiation which causes impedance mismatching and gain decreasing. Moreover, the in-phase superposition of the induced currents

furtherly aggravates the influence on the LB antenna’s performance. Fortunately, there is an effective way to suppress the common-mode current using ferrite material in power delivery applications [21], [22]. Therefore, we innovatively implement ferrite choke rings in dual-band antenna array design. As shown in Fig. 5(b), the ferrite choke rings with double holes serve as magnetic sleeves for the coaxial cables. Each hole serves as a pipeline to let one coaxial cable pass through. The ferrite choke ring is vertically mounted on the ground plane and the total height is equal to the distance between the FSS and the ground plane. According to the law of Lenz, an induced electromotive force (EMF) will be excited when a time-varying current passes through a magnet. In the common-mode current situation, the induced EMF produced by one of the coaxial cables suppresses the current on the other coaxial cable. Meanwhile, the high relative permeability of the ferrite choke rings ( $\mu_r \approx 2000$ ) ensures that the common-mode current will be suppressed to a low level. As shown in Fig. 5(b), the induced currents on the coaxial cables become weak enough as compared with the currents shown in Fig. 5(a). As illustrated in Fig. 4(c), with the ferrite choke rings introduced around each pair of coaxial cables, the deterioration in the radiation patterns of the LB antenna vanishes and the XPD are improved. The gain is higher than 8 dBi and the XPD is improved to higher than 21 dB over the entire LB.

### C. APPLICATIONS OF THE BAFFLE STRUCTURES

The final challenge is to suppress the in-band mutual coupling within the UB antenna array. Fig. 6 shows the configuration of the antenna array with the proposed baffle structures. The UB antenna array in this work is a  $4 \times 4$  dual-polarized dipole antenna array with a compact element spacing distance of  $43 \text{ mm} \times 62.5 \text{ mm}$  (center to center distance). The traditional metal ground of the UB antenna array is replaced by the FSS surface designed in Part A. Typical antenna ports



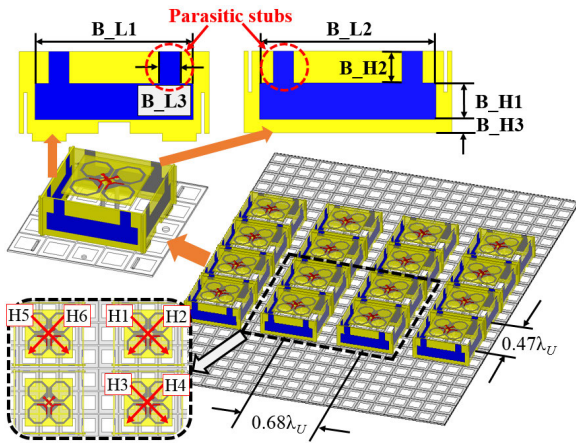


FIGURE 6. Configuration of the UB MIMO antenna array with the proposed baffle structures.

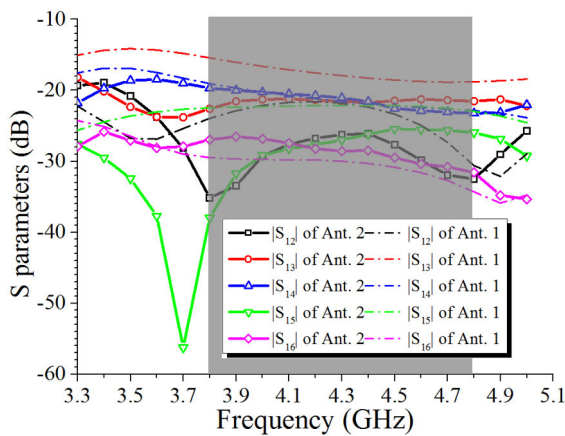


FIGURE 7. Comparisons of port-to-port coupling in antenna array without baffle structures (Ant. 1) and antenna array with baffle structures (Ant. 2).

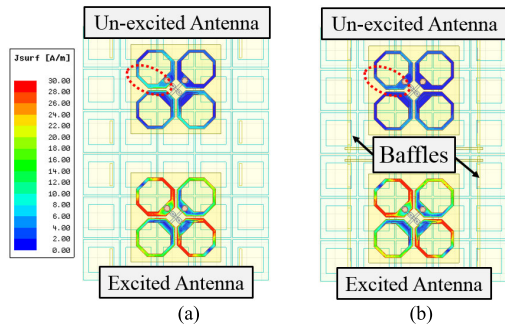
are labelled with H1-H6. Coupling coefficients between port 1 to port 2~6 are presented in Fig. 7. The intended frequency bands range from 3.3-3.8 GHz and 4.8-5.0 GHz. The unintended frequency band from 3.8 GHz to 4.8 GHz has been shadowed in the flowing figures. In the antenna array without decoupling step (Ant 1), the highest coupling coefficient occurs at two co-polarization ports in the direction of the narrow side (port 1 and port 3). The  $|S_{13}|$  is around  $-14$  dB at 3.6 GHz because the smallest edge-to-edge distance between the adjacent antennas is only 13 mm ( $0.14\lambda_U$ ). Meanwhile, mutual coupling between cross-polarization ports (port 1 and port 4) is higher than  $-18$  dB below 3.8 GHz. Evidently, in-band decoupling technology must be introduced to reduce the mutual coupling among antenna elements.

Mutual coupling suppressing in MIMO antenna systems has attracted intense attention of the literature for decades. Numerous decoupling methods based on metamaterial structures have been studied in variety types of antennas. EM bandgap structures have been applied in [23]–[25] for dense patch antenna arrays with antenna element numbers

varied from 2 to 6. The decoupling structures in these works are all planar slabs with slots or holes etched on them. Owing to the bandgap property of the metamaterial slab, significant decoupling effects are achieved in these patch antenna arrays. It is easier to suppress mutual coupling in microstrip antenna array than in 3D antenna array due to the EM coupling in patch arrays is governed by surface waves (or surface currents). However, in 3D dipole antenna arrays, spatial EM coupling spreads in space around each antenna element, which makes decoupling process more complicate. In recent years, metamaterial surfaces [26], [27] and cavity structures [28] have been proposed to deal with the mutual coupling problems in 3D dipole antenna array. Unfortunately, the meta-surface is limited by single polarization [26] and increased profile height [27]. The cavity structure needs large volume with element spacing distance greater than one wavelength [28].

To compromise the performance of the port-to-port decoupling and maintain a compact size design, a baffle configuration is designed in this work. The baffle configuration is shown in Fig. 6. The yellow area is the dielectric substrate without PEC patch covering, while the blue area is covered with PEC patches. As compared with traditional baffles that are usually soldered on the ground plane, the proposed baffle structure is printed on a dielectric sheet and is not directly soldered with the FSS. Therefore, it allows the baffle structure to sit across several FSS unit cells. The frequency responses of the FSS will not be influenced by the baffle structure. Furthermore, the baffle is constructed by four separated metallic strips to ensure that the decoupling structure won't strongly influence the radiation performance of the UB antenna. The height and the length of the metallic strips are optimized to balance the reduction on coupling coefficients and the influence on impedance matching performance. Two parasitic stubs are introduced over each strip to further reduce the mutual coupling. The locations of these two parasitic stubs could be optimized to minimize the influence on radiation patterns while maintain good decoupling effect. The solid lines in Fig. 7 shows the simulated port-to-port coupling coefficient of the antenna array with the proposed baffles (Ant. 2). The  $|S_{13}|$  is reduced by at least 4 dB. At 3.6 GHz, the  $|S_{13}|$  is reduced from  $-15$  dB to  $-24.5$  dB with the largest reduction of 9.5 dB. The  $|S_{13}|$  and the  $|S_{14}|$  are reduced to less than  $-18$  dB from 3.3 to 3.8 GHz. Meanwhile, the coupling coefficients are all below than  $-20$  dB between 4.8 to 5.0 GHz. The  $|S_{12}|$  is influenced by the decoupling baffles below 3.6 GHz. However, the  $|S_{12}|$  lower than  $-18$  dB is still sufficient for MIMO applications.

To reveal the operation mechanism of the baffle structures, Fig. 8 compares the current distributions in Ant. 1 and Ant. 2 at 3.6 GHz. For the case without baffles as indicated in Fig. 8 (a), large current density is induced over the radiation arms of the excited and the adjacent un-excited antenna elements. The strongest currents on the un-excited antenna follow in the same polarization with the excited antenna, which consistent with the strongest mutual coupling appeared


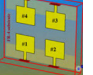
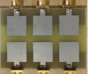
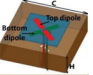

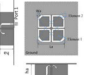
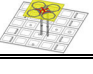


**FIGURE 8.** Comparison of current distribution on the adjacent antennas at 3.6 GHz. (a) Without baffles; (b) with baffles.

between two co-polarization antenna ports. By introducing baffle structures among the antenna elements, the current distributions on the excited antenna are the same with Fig. 8(a). The induced currents on the adjacent antenna element are minimized, as shown in Fig. 8 (b). Therefore, the designed baffle structure could reduce the mutual coupling between adjacent antenna elements while keep the performance of the working antenna.

To clearly illustrate the decoupling effect owing to the designed baffles, Table 1 compares the mutual coupling coefficients of the proposed antenna array with the state-of-the-art MIMO antenna array designs. The second column of the TABLE 1 shows the configuration of antenna without decoupling structure in each work. The antenna elements in [23]–[25] are microstrip antenna while the antennas in [4], [27], [29] are 3D dual-polarized cross-dipole antennas. The third column presents the center-to-center distance in each compared array while the wavelength  $\lambda_{UL}$  is calculated

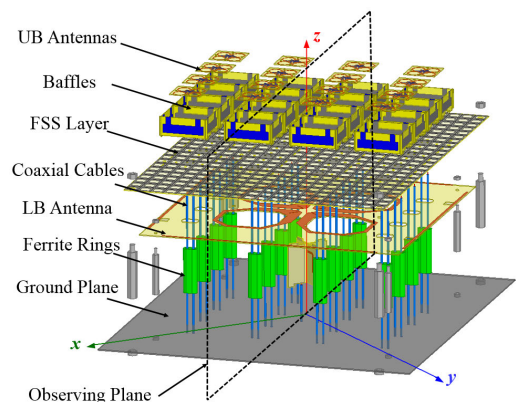
**TABLE 1.** Comparison of the coupling coefficients of various designs.

Refs.	Antenna element	Element Spacing	Bandwidth	Mutual Coupling
[23]		$1.24\lambda_{UL}$	119%	< -28 dB
[24]		$1.52\lambda_{UL} \times 1.67\lambda_{UL}$	8.8%	< -28 dB
[25]		$0.62\lambda_{UL} \times 0.62\lambda_{UL}$	17.3%	< -11 dB
[4]		$0.49\lambda_{UL} \times 0.49\lambda_{UL}$	20.2%	< -13 dB
[29]		$0.47\lambda_{UL} \times 0.68\lambda_{UL}$	24%	< -15.5 dB
[27]		$0.49\lambda_{UL} \times 0.66\lambda_{UL}$	14.1%	< -23 dB
This work		$0.47\lambda_{UL} \times 0.68\lambda_{UL}$	40.9%	< -18 dB

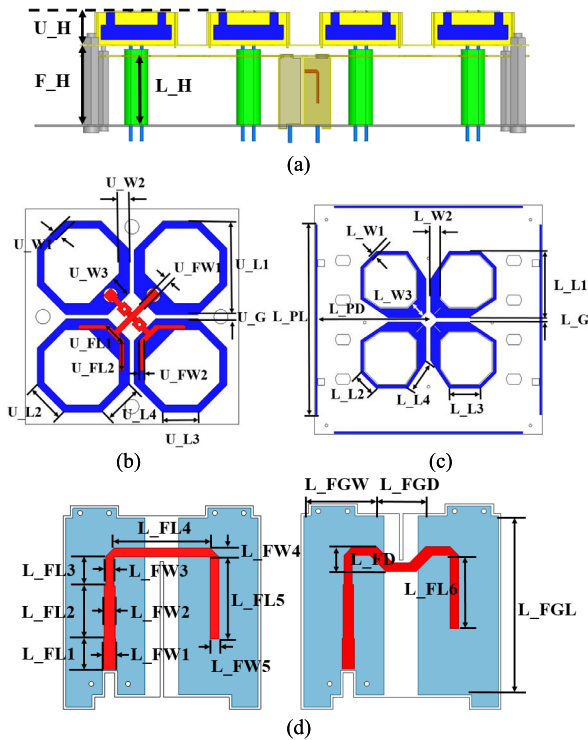
at the lowest operation frequency in each design. The last column is the maximum coupling coefficient achieved by applying the corresponding decoupling methods. As shown in TABLE 1, the best mutual coupling is achieved in [23] and [24] with coupling coefficient lower than -28 dB. However, the element spacing distances in these two works are larger than one wavelength. In sub-6 GHz MIMO antenna arrays, the interval distances are usually restricted to  $0.4\lambda_{UL}$  to  $0.6\lambda_{UL}$ . As can be seen from [25], the antenna elements are strongly coupled in a densely patched microstrip antenna array due to surface wave. The worst coupling coefficient is only -11 dB even though the EM bandgap decoupling slab has been applied in this array. For 3D dual-polarized dipole antenna array, it can be seen that the coupling coefficient would be as high as -13 dB if additional decoupling structures were not introduced [4]. Parasitic element is implemented in [29] but the worst coupling coefficient is only reduced to -15.5 dB. The lowest coupling coefficient is realized by the work in [27], however, the profile height is increased. Therefore, the proposed antenna array with specially designed baffle structures compromises the performance of the port-to-port decoupling and maintain a compact size design.

**D. CONFIGURATIONS OF THE PROPOSED ANTENNA ARRAY**

Fig. 9 presents the configuration of the dual-band antenna array that incorporates all the decoupling techniques discussed previously. As mentioned before, the UB antenna array is a planar array with large number of antenna elements. It is not appropriate to use the tradition embedded layout to achieve dual-band operation. Therefore, the three-layer configuration is introduced in [18] and this work. The top layer consists of the dual-polarized UB MIMO array with its decoupling baffles designed in Part C. The middle layer is the isolation FSS consisting by rectangular ring unit cells as described in Part A. The bottom layer contains the LB antenna, the ground plane, and the ferrite chock rings which has been discussed in Section B. The novelty of this layout is:



**FIGURE 9.** The exploded 3D view of the proposed dual-band antenna array.



**FIGURE 10.** Geometry of the proposed dual-band dual-polarized antenna array. (a) Side view of the antenna array; (b) top view of the UB antenna; (c) top view of the LB antenna; (d) the  $\Gamma$ -shaped balun for the LB antenna.

i) the UB antennas are free of the parasitic coupling problems with the LB antenna. They are placed above the LB antenna and the FSS inserted below them reflects most of the UB EM waves to the upper free space; ii) the LB antenna radiates efficiently under the FSS due to the FSS being penetrable for the LB EM wave and the coaxial cables have been well decoupled from the LB antenna with the ferrite chock rings; iii) the whole structure is in compact size since the LB antenna achieves low-profile features.

Fig. 10 shows the geometry of the proposed dual-band dual-polarized antenna array. Both the LB and UB antenna elements are composed of a pair of loop-shaped dipoles which have been extensively studied for dual-polarization purpose [30]–[33]. The blue areas in Fig. 10(b) and (c) are radiation patches of the LB and UB antennas printed on the bottom side of the substrate. The red lines in Fig. 10(b) are Y-shaped feeding lines to provide capacitive coupling excitation for the UB antenna [32]. The inner conductor of the coaxial cable is soldered to the Y-shaped feeding line, while the outer conductor of the coaxial cable is soldered to one of the dipole arms. As for the LB antenna, the feeding structures are two perpendicularly placed  $\Gamma$ -shaped baluns shown in Fig. 10(d). The blue areas in Fig. 10(d) are ground planes printed on the bottom side of the substrate while the red lines are the tapered transmission lines to achieve broadband impedance matching. The baluns are vertically mounted between the LB antenna and the ground plane.

**TABLE 2.** Dimensions of the proposed dual-band antenna array.

Parameter	Value (mm)	Parameter	Value (mm)	Parameter	Value (mm)
U_H	18	B_H3	3	L_G	5
U_G	0.63	F_H	44	L_FGW	16.5
U_L1	13	F_L1	12	L_FGL	36.5
U_L2	5.3	F_L2	13.6	L_FGD	7
U_L3	5.2	F_W1	2.6	L_FD	5.1
U_L4	5.65	F_W2	1.7	L_FL1	12
U_W1	1	F_G1	0.7	L_FL2	11
U_W2	1.5	F_G2	0.5	L_FL3	6
U_W3	3	L_H	38	L_FL4	20
U_FL1	3	L_L1	72	L_FL5	17
U_FL2	4	L_L2	24	L_FL6	15
U_FW1	0.8	L_L3	35	FW1_L	2.5
U_FW2	0.6	L_L4	36	FW2_L	2.2
B_L1	34.8	L_W1	3.5	FW3_L	1.7
B_L2	39	L_W2	11	FW4_L	1.8
B_L3	4.5	L_W3	17	FW5_L	1.8
B_H1	8	L_PL	207		
B_H2	7	L_PD	122		

Moreover, there are four parasitic strips along the periphery of the crossed dipoles to improve the XPD [34], as shown in Fig 10(c). The offset distance of the parasitic strips from the center of the antenna is around  $0.34\lambda_L$ . The length of each parasitic element is  $0.3\lambda_L$ .

In addition, all of the LB and UB dipole antennas, the baluns for the LB antennas, and the baffle structures for the UB antenna array are printed on RF-30 dielectric substrates ( $\epsilon_r = 3.0$ ) with a thickness of 0.762 mm. The FSS layer is fabricated from a 0.635 mm thick RF-10 dielectric substrate ( $\epsilon_r = 10.2$ ) with the size of 344 mm  $\times$  250 mm. The size of the ground plane is 344 mm  $\times$  344 mm. The total profile height of the dual-band antenna array is 63 mm, which is only  $0.17\lambda_L$ . The detailed dimensions of the antenna array are presented in TABLE 2.

In summary, a dual-band shared-aperture MIMO antenna array for 5G base station applications is developed in this section. To address the problems caused by the rectangular antenna array lattice and the additional coupling problem introduced by the coaxial cables, decoupling techniques including rectangular FSS unit cell, ferrite chock ring, and baffle structure are implemented together in the design. The contributions of this work are summarized as follows,

- a) To the best of the authors’ knowledge, it is the first time to realize a dual-band shared-aperture MIMO antenna array that consists of a  $4 \times 4$  sub-6 GHz antenna array and a GSM-900 band antenna. All the antenna elements work properly and possess stable radiation patterns in such a crowded antenna array environment.



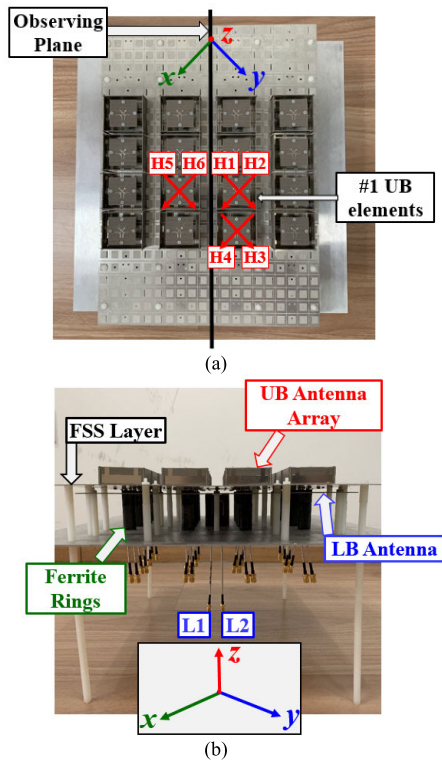


FIGURE 11. The fabricated prototype of the proposed dual-band antenna array. (a) Top view; (b) side view.

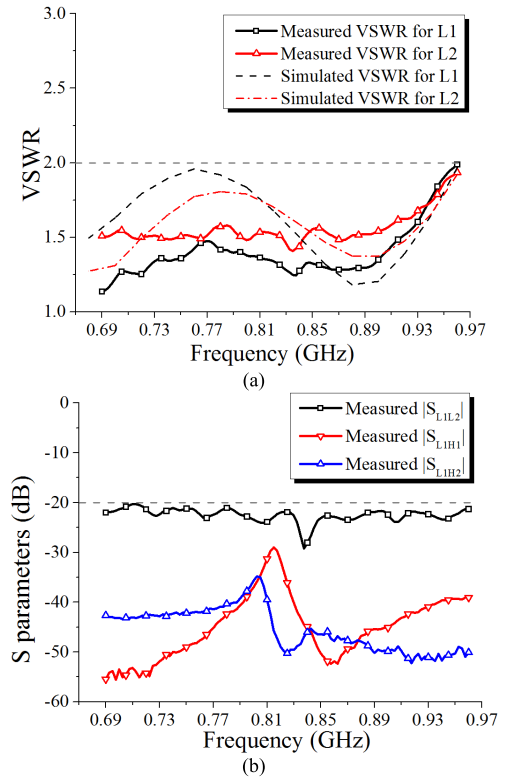


FIGURE 12. Port characteristics of the LB antenna: (a) Simulated and measured VSWR for L1 (+45° port) and L2 (-45° port) antennas; (b) port coupling coefficients between L1 port and other ports.

- b) It is also the first time to achieve decoupling effect for sub-6 GHz and GSM band antenna by simultaneously employing three decoupling technologies. The cross-band coupling issues between the LB and UB antenna have been well addressed by the FSS with the rectangular ring unit cells and the ferrite chock rings. The in-band mutual coupling is suppressed to a satisfactory level due to the proposed baffle structures.
- c) Owing to the UB-FSS-LB topology, the proposed antenna array achieves a lower profile height compared to the dual-band base station antenna reported in the literature.

### III. PERFORMANCE OF THE DUAL-BAND ANTENNA ARRAYS

Fabricated prototype with the ports labels is shown in Fig. 11(a) and (b). There are totally 32 ports for the UB antenna array and 2 ports for the LB antenna. For brevity, only 6 UB antenna ports (H1 to H6) and 2 LB antenna ports (L1 and L2) are presented in the following discussions.

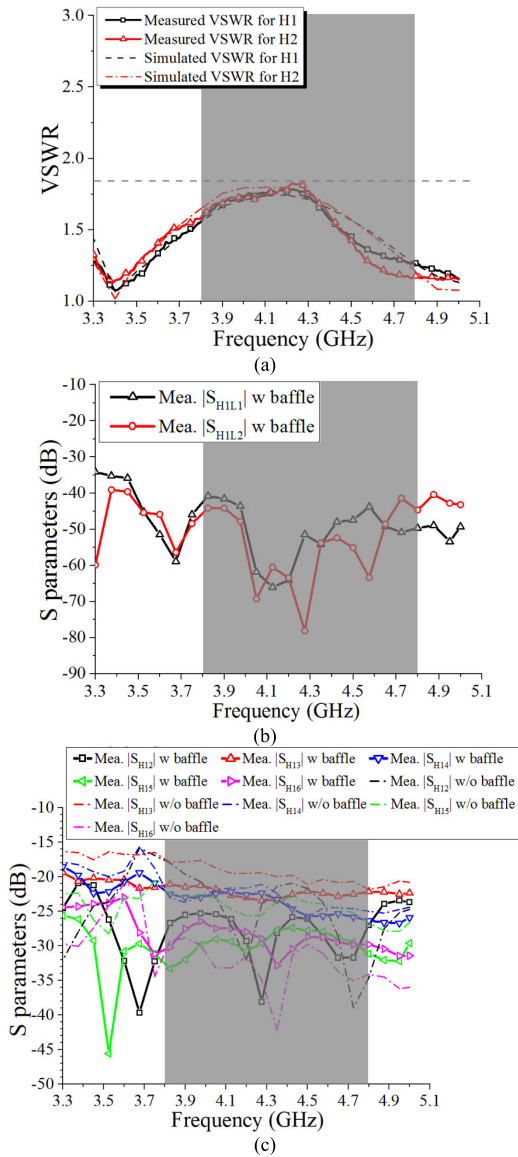
Fig. 12(a) presents the simulated and measured VSWRs of the L1 (+45° port) and L2 (-45° port) ports. Both of the simulated and measured impedance bandwidths cover the frequency range of 0.69-0.96 GHz for VSWR < 2.0. The lower reflection coefficient appeared in measurement is due to fabrication errors and the loss of coaxial cables are not entirely considered in simulations. Fig. 12(b) shows the coupling coefficients between the L1 and L2 ports is less than

-20 dB, which means the radiation energy from two orthogonally polarized antennas is coupled very weakly. Due to the decoupling effect of the FSS, the coupling coefficients between LB antenna ports and UB antenna ports are less than -30 dB, which means the LB antenna and the UB antenna is well decoupled in the lower frequency band.

Because of the symmetry property of the 4 × 4 UB antenna array, only the VSWRs of ports labeled with H1 and H2 are presented in Fig. 13(a). The #1 UB antenna covers the frequency range of 3.3-5 GHz for VSWR < 1.8. The measured cross-band coupling coefficients from 3.3 to 5.0 GHz are shown in Fig. 13(b). Owing to the isolation function of the FSS, the mutual coupling between the LB and UB antenna in the UB are lower than -34 dB, which indicates the LB antenna and the UB antenna are also well decoupled in the upper frequency band. The coupling coefficients of the UB antenna array with and without baffles are presented in Fig. 13(c). From the dash lines, the largest coupling coefficient in the case without baffles is nearly -15 dB. The |S<sub>L13</sub>| and |S<sub>L14</sub>| are higher than -20 dB in the frequency range of 3.3-3.8 GHz. When the proposed baffles are mounted on UB antenna array, the largest coupling coefficient is reduced to -18.5 dB and rest of them are lower than -20 dB over the entire UB.

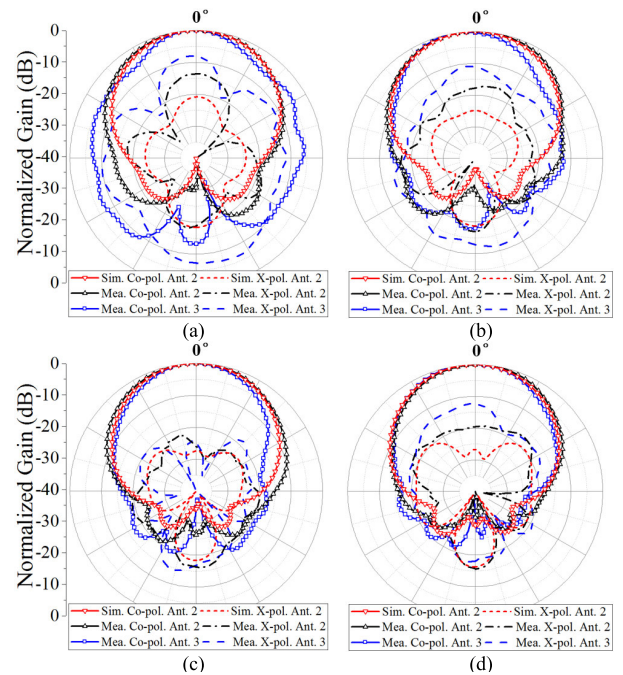
Fig. 14 shows the measured and simulated radiation patterns when L1 port is excited. The observation plane is





**FIGURE 13.** Port characteristics of the UB antenna array: (a) Simulated and measured VSWR for H1 (+45° port) and H2 (-45° port) antennas; (b) in-band coupling coefficients between H1 port and other UB antenna ports; (c) cross-band coupling coefficients between H1 port and LB antenna ports.

the  $\varphi = 45^\circ$  plane shown in Fig. 9 and Fig 11(a). The proposed antenna (Ant. 2) and the prototype without ferrite chock rings (Ant. 3) are fabricated and measured to validate the common-mode currents suppression effects of the ferrite chock rings. The blue line in Fig. 14(a) shows a severe radiation pattern deterioration caused by the coaxial cables of the UB antenna array at 0.69 GHz. The co-polarization component is distorted and the cross polarization is raised to a high level of  $-7$  dB. The influences can be also observed at 0.76 GHz for both co- and cross-polarization. The XPD at 0.96 GHz is also influenced by the coaxial cables. From the radiation pattern of Ant. 3, the coaxial cables are indeed coupled with the LB antenna and the radiation performances

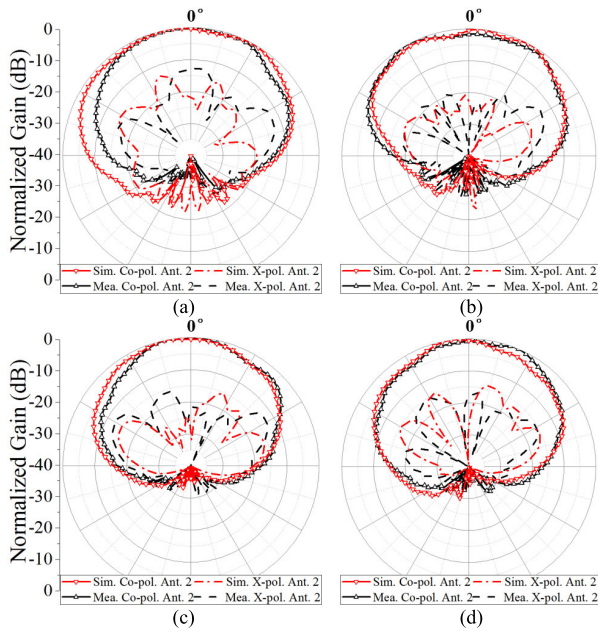


**FIGURE 14.** Simulated and measured normalized radiation patterns of the LB antenna with +45° polarization. (a) 0.69 GHz; (b) 0.76 GHz; (c) 0.86 GHz; (d) 0.96 GHz.

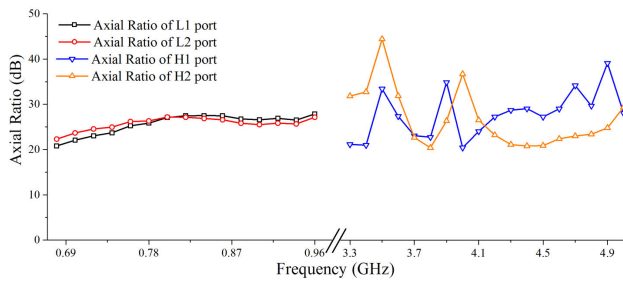
of the LB antenna are destroyed. However, when ferrite chock rings are introduced for each pair of coaxial cables, the measured and simulated co-polarization patterns agree well with each other from 0.69 GHz to 0.96 GHz, and the radiation pattern deterioration disappears. The XPDs of the Ant. 2 are higher than 14 dB in measurements and higher than 20 dB in simulations. Due to the limited accuracy in low power level measurement and the errors in assemble, some slight discrepancy appears between the simulated and measured cross polarization patterns.

The radiation patterns of the UB antenna for H1 port excited are presented in Fig. 15. Due to the isolation effect of the FSS, the co-polarization components shown in Fig. 15 are quite stable and there are no evident ripples in co-polarization patterns over the entire operation frequency band. The discrepancy of the cross-polarization patterns is caused by the un-flatness of the FSS in the fabrication model. On the contrary, it is very hard to achieve such stable radiation patterns for the UB antennas in the traditional embedded layout. The simulation results of the UB antenna in embedded layout have been presented in [18], which shows that the LB antenna severely influences the UB antenna in both radiation performance and impedance matching.

To justify the linear-polarized quality of each polarization in each antenna, the axial ratios (ARs) of the LB and UB antennas are provided in Fig. 16. AR is a radiation pattern parameter that measures the circularly polarization ability of the antenna. It is defined as the ratio of the major to the minor axis of the polarization ellipse. The value of AR close to 0 dB means the antenna is circularly polarized. On the contrary,



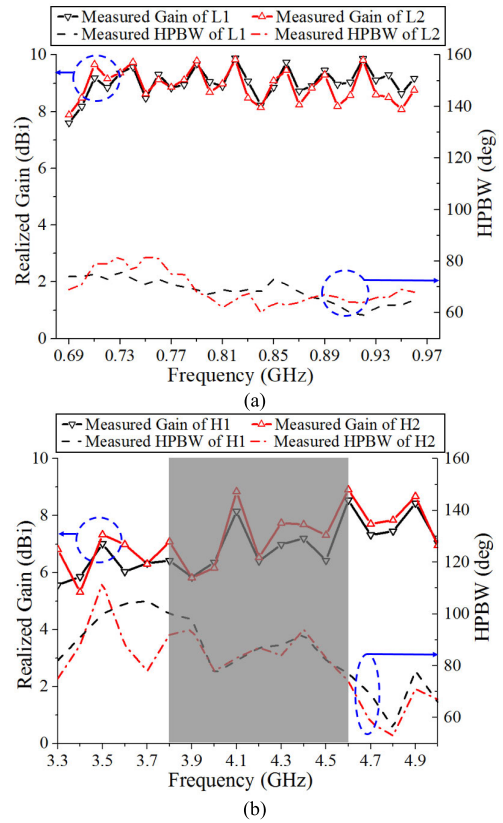
**FIGURE 15.** Simulated and measured normalized radiation patterns for the UB antennas with +45° polarization. (a) 3.3 GHz; (b) 3.8 GHz; (c) 4.8 GHz; (d) 5.0 GHz.



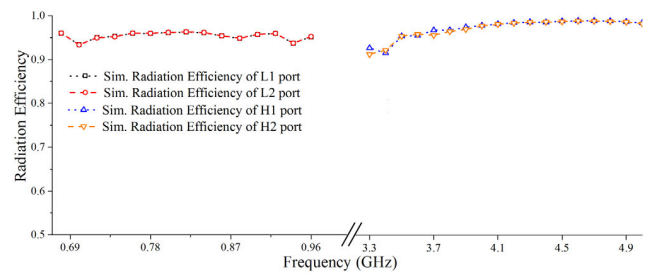
**FIGURE 16.** Axial ratio of the proposed dual-band antenna array.

the large value of AR means the antenna is linear polarized. As shown in Fig. 16, the ARs for the LB and UB antennas vary from 20 dB to 50 dB in both  $\pm 45^\circ$  polarizations. It indicates that the strength of the major axis component is at least 100 times stronger than the minor axis component. The radiation fields of the LB and UB antenna are qualified to be seen as linear polarized and the proposed decoupling structures do not destroy the dual-linear-polarization property of the LB and UB antennas.

Fig. 17 presents the realized gains at  $0^\circ$  and half power beamwidths (HPBW) of the proposed antennas. The gains of the dual-band antenna array are  $8.6 \pm 1.2$  dBi and  $7.3 \pm 1.7$  dBi in the two frequency bands, respectively. The lowest gain is 7.8 dB for the LB antenna at 0.69 GHz and the lowest gain is 5.5 dB for the UB antenna at 3.4 GHz. Due to the UB antenna is surrounded by the decoupling baffle structure, the HPBW of the UB antenna is broaden. This results in a lower gain at  $0^\circ$  compared to the LB antenna. The measured HPBWs are around  $74^\circ$  in the LB and  $88^\circ$  in the UB, which satisfy the practical requirements in base station applications.



**FIGURE 17.** Measured realized gains and HPBWs for the (a) LB antenna and (b) UB antennas.



**FIGURE 18.** Radiation efficiency of the proposed dual-band antenna array.

Fig.18 shows the simulated radiation efficiencies in both bands. The simulated efficiencies are higher than 90% for both LB and UB antennas. The average radiation efficiency for LB antenna is 95.4% while the average radiation efficiency for UB antenna is 96%. From the simulated results there is no significant loss introduced by the proposed decoupling technologies. The radiation efficiency of the fabricated antenna is not measured due to the transverse size of the proposed antenna is  $344 \text{ mm} \times 344 \text{ mm}$ , which is too large to be mounted in near-field SATIMO anechoic chamber. Moreover, the SATIMO system is operating at frequencies higher than 1 GHz, which further limits us to get accurate measured results. Nevertheless, good radiation efficiency can be concluded from measured impedance matching and realized gain shown in Fig. 17. High gain and well matched performance

TABLE 3. Proposed antenna characteristics compared with other works.

Refs.	Antenna Schemes	Configuration of HB antenna array	Number of HB antenna Overlapped with LB antenna	Bandwidth of LB antenna	Bandwidth of HB antenna	Frequency Band Ratio (HB/LB)	Profile Height
[8]	Embedded	Linear	1	15.7%	23.7%	2.2	$0.22\lambda_{CL}$
[9]	Embedded	Linear	1	21.2%	28.4%	2.2	Not given
[10]	Embedded	Linear	2	20%	60%	2.5	$0.13\lambda_{CL}$
[11]	Embedded	Linear	1	23.5%	50.9%	2.5	$0.23\lambda_{CL}$
[12]	Embedded	Linear	1	31.6%	45.5%	2.6	$0.25\lambda_{CL}$
[15]	Embedded	Linear	1	7.3%	8.7%	1.3	$0.26\lambda_{CL}$
[7]	Vertically Placed	Linear	1	20.4%	29.3%	2.1	$0.35\lambda_{CL}$
[13]	Vertically Placed	Linear	1	32.7%	44.5%	2.6	$0.23\lambda_{CL}$
[14]	Vertically Placed	Linear	1	32.7%	44.5%	2.6	$0.21\lambda_{CL}$
[17]	Fragmental Dipole	Planar	4	19.7%	28.5%	2.6	$0.30\lambda_{CL}$
This work	UB-FSS-LB	Planar	16	32.7%	41%	5.0	$0.17\lambda_{CL}$

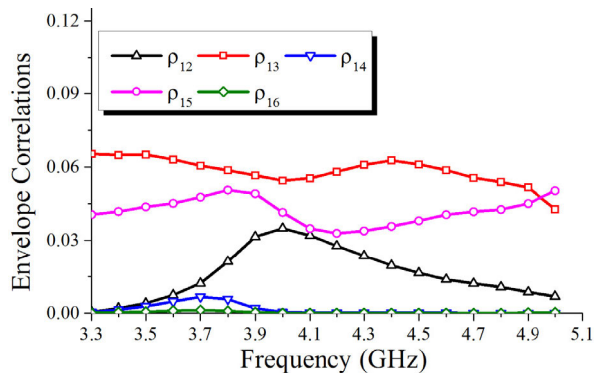


FIGURE 19. Envelope correlation coefficient of the UB antenna array.

prove that most of input energy is efficiently radiated from the proposed antenna structure to the free space.

Diversity of the presented MIMO antenna array is validated from envelope correlation coefficient (ECC). Due to the large number of the UB antenna ports, it is more convenient to calculate the ECC from radiation patterns. The 3D far field patterns are extracted from simulation and the ECCs between port 1 to port 2~6 are presented in Fig. 19. Owing to the stable radiation pattern and high port-to-port isolation, all the ECCs are less than 0.1 which satisfy the general criteria of  $ECC < 0.3$  in base station systems.

It is worthy to mention that the goal of this paper is to achieve stable radiation patterns for both LB and UB antenna elements in a crowded antenna array environment. Satisfactory beam performance of antenna array could be guaranteed by the stable radiation patterns of each antenna element and the well decoupled mutual coupling among antenna elements. The measurement results have already demonstrated the stable radiation patterns in the UB band antennas as well as the low mutual coupling among them. Therefore, the beam property of the UB antenna array is not analyzed in this paper.

In summary, both the simulated and measured results demonstrate the effectiveness of the three decoupling techniques as well as the UB-FSS-LB shared-aperture strategy.

IV. COMPARISON WITH OTHER DUAL-BAND ANTENNAS

The proposed antenna array is compared with other dual-band antennas in TABLE 3. Each antenna listed in TABLE 3 is designed for dual-band base station application with one lower-band (LB) antenna array and one higher-band (HB) antenna array. As can be seen, most HB antenna arrays considered in literature are linear antenna array. Moreover, there is usually only one HB antenna overlapped with one LB antenna, which ease the decoupling issues across the two bands. The number of the overlapped HB antenna in [10] is greater than one and the total profile height is the lowest ( $\lambda_{CL}$  is the wavelength of the center frequency of the LB). However, the LB and UB antennas in [10] are single-polarized antennas and the array layout cannot be implemented into dual-polarized antenna arrays. Similarly, four HB antenna elements achieve shared-aperture working property with one LB antenna in [17]. However, the bandwidth of the LB antenna is very limited due to the radiation patches of the LB dipole are fragmented to reduce the mutual coupling with the HB antennas. From the comparison, the UB-FSS-LB layout is the only approach that achieves shared-aperture working for large number of HB antennas. Meanwhile, both the LB and HB antenna in this work possesses full-band operation performances due to three innovatively introduced decoupling technologies. The profile height of the designed antenna array is also lower than the most of the state of the art dual-band base station antennas.

V. CONCLUSION

A shared-aperture dual-band dual-polarized 5G MIMO antenna array is developed in this paper. The rectangular



array layout, the induced current on coaxial cables, and the mutual coupling in closely spaced antenna array increase the design complexity. Three decoupling techniques, including the FSS with rectangular ring unit cells, ferrite chock rings, and baffle structures are introduced to overcome the challenges. The simulation results show the proposed antenna achieves VSWR lower than 2 and mutual coupling coefficients lower than  $-20$  dB in both bands. The gains are higher than 8 dBi and 6 dBi for the LB and UB antenna, respectively. The radiation efficiencies for the LB and the UB antenna are both higher than 90%. The measured results validate the port characteristics and the radiation performances of the proposed dual-band antenna array. In addition, the total height of the antenna array is  $0.17\lambda_L$  which is much lower than the state of the art dual-band base station antennas. Therefore, the proposed decoupling strategies provide hopeful solutions for low-profile, compact, and shared-aperture 5G massive MIMO base station antenna array developments.

## REFERENCES

- [1] E. G. Larsson, O. Edfors, F. Tufvesson, and T. L. Marzetta, "Massive MIMO for next generation wireless systems," *IEEE Commun. Mag.*, vol. 52, no. 2, pp. 186–195, Feb. 2014.
- [2] P. Xingdong, H. Wei, Y. Tianyang, and L. Linsheng, "Design and implementation of an active multibeam antenna system with 64 RF channels and 256 antenna elements for massive MIMO application in 5G wireless communications," *China Commun.*, vol. 11, no. 11, pp. 16–23, Nov. 2014.
- [3] Y. Gao, R. Ma, Y. Wang, Q. Zhang, and C. Parini, "Stacked patch antenna with dual-polarization and low mutual coupling for massive MIMO," *IEEE Trans. Antennas Propag.*, vol. 64, no. 10, pp. 4544–4549, Oct. 2016.
- [4] M. V. Komandla, G. Mishra, and S. K. Sharma, "Investigations on dual slant polarized cavity-backed massive MIMO antenna panel with beam-forming," *IEEE Trans. Antennas Propag.*, vol. 65, no. 12, pp. 6794–6799, Dec. 2017.
- [5] A. Alieldin, Y. Huang, M. Stanley, S. D. Joseph, and D. Lei, "A 5G MIMO antenna for broadcast and traffic communication topologies based on Pseudo inverse synthesis," *IEEE Access*, vol. 6, pp. 65935–65944, 2018.
- [6] X. Liu, S. He, H. Zhou, J. Xie, and H. Wang, "A novel low-profile, dual-band, dual-polarization broadband array antenna for 2G/3G base station," in *Proc. IET Int. Conf. Wireless, Mobile Multimedia Netw.*, Nov. 2006, pp. 1–5.
- [7] M. Kabolli, M. S. Abrishamian, S. A. Mirtaheri, and S. M. Aboutorab, "High-isolation XX-polar antenna," *IEEE Trans. Antennas Propag.*, vol. 60, no. 9, pp. 4046–4055, Sep. 2012.
- [8] Y. He, Z. Pan, X. Cheng, Y. He, J. Qiao, and M. M. Tentzeris, "A novel dual-band, dual-polarized, miniaturized and low-profile base station antenna," *IEEE Trans. Antennas Propag.*, vol. 63, no. 12, pp. 5399–5408, Dec. 2015.
- [9] S. Chen and K.-M. Luk, "High performance dual-band dual-polarized magneto-electric dipole base station antenna," in *Proc. Asia-Pacific Microw. Conf. (APMC)*, Nov. 2014, pp. 321–323.
- [10] Y. Cui, R. Li, and P. Wang, "Novel dual-broadband planar antenna and its array for 2G/3G/LTE base stations," *IEEE Trans. Antennas Propag.*, vol. 61, no. 3, pp. 1132–1139, Mar. 2013.
- [11] H. Huang, Y. Liu, and S. Gong, "A novel dual-broadband and dual-polarized antenna for 2G/3G/LTE base stations," *IEEE Trans. Antennas Propag.*, vol. 64, no. 9, pp. 4113–4118, Sep. 2016.
- [12] R. Wu and Q. Chu, "A compact, dual-polarized multiband array for 2G/3G/4G base stations," *IEEE Trans. Antennas Propag.*, vol. 67, no. 4, pp. 2298–2304, Apr. 2019.
- [13] W. Wu, H. Peng, and J. Mao, "A new compact dual-polarized co-axial full-band antenna for 2G/3G/LTE base station applications," in *Proc. IEEE Electr. Design Adv. Packag. Syst. Symp. (EDAPS)*, Dec. 2017, pp. 1–3.
- [14] H. Huang, X. Li, and Y. Liu, "A novel vector synthetic dipole antenna and its common aperture array," *IEEE Trans. Antennas Propag.*, vol. 66, no. 6, pp. 3183–3188, Jun. 2018.
- [15] Y. Liu, S. Wang, N. Li, J.-B. Wang, and J. Zhao, "A compact dual-band dual-polarized antenna with filtering structures for Sub-6 GHz base station applications," *IEEE Antennas Wireless Propag. Lett.*, vol. 17, no. 10, pp. 1764–1768, Oct. 2018.
- [16] A. Alieldin, Y. Huang, S. Boyes, M. Stanley, S. D. Joseph, Q. Hua, and D. Lei, "A triple-band dual-polarized indoor base station antenna for 2G, 3G, 4G and sub-6 GHz 5G applications," *IEEE Access*, vol. 6, pp. 49209–49216, 2018.
- [17] H.-H. Sun, C. Ding, H. Zhu, B. Jones, and Y. J. Guo, "Suppression of cross-band scattering in multiband antenna arrays," *IEEE Trans. Antennas Propag.*, vol. 67, no. 4, pp. 2379–2389, Apr. 2019.
- [18] Y. Zhu, Y. Chen, and S. Yang, "Decoupling and low-profile design of dual-band dual-polarized base station antennas using frequency-selective surface," *IEEE Trans. Antennas Propag.*, vol. 67, no. 8, pp. 5272–5281, Aug. 2019.
- [19] D. Ferreira, R. F. S. Caldeirinha, I. Cuinas, and T. R. Fernandes, "Square loop and slot frequency selective surfaces study for equivalent circuit model optimization," *IEEE Trans. Antennas Propag.*, vol. 63, no. 9, pp. 3947–3955, Sep. 2015.
- [20] N. Liu, X. Sheng, C. Zhang, J. Fan, and D. Guo, "A design method for synthesizing wideband band-stop FSS via its equivalent circuit model," *IEEE Antennas Wireless Propag. Lett.*, vol. 16, pp. 2721–2725, 2017.
- [21] S. Shahabi and A. Gholami, "Mitigation of switching-induced transient electromagnetic interference on control cable using ni-zn ferrite rings over cable sheath in gas-insulated substations," *IEEE Trans. Electr. Electron. Eng.*, vol. 8, no. S1, pp. S5–S12, 2013.
- [22] J. He, Y. Guan, W. Liu, W. Chen, and Z. Li, "Design optimization of ferrite rings for VFTO mitigation," *IEEE Trans. Power Del.*, vol. 32, no. 3, pp. 1181–1186, Jun. 2017.
- [23] M. Alibakhshikenari, M. Khalily, B. S. Virdee, C. H. See, R. A. Abd-Alhameed, and E. Limiti, "Mutual coupling suppression between two closely placed microstrip patches using EM-bandgap metamaterial fractal loading," *IEEE Access*, vol. 7, pp. 23606–23614, 2019.
- [24] M. Alibakhshikenari, M. Khalily, B. S. Virdee, C. H. See, R. A. Abd-Alhameed, and E. Limiti, "Mutual-coupling isolation using embedded metamaterial EM bandgap decoupling slab for densely packed array antennas," *IEEE Access*, vol. 7, pp. 51827–51840, 2019.
- [25] M. Alibakhshikenari, B. S. Virdee, P. Shukla, C. H. See, R. A. Abd-Alhameed, F. Falcone, K. Quazzane, and E. Limiti, "Isolation enhancement of densely packed array antennas with periodic MTM-photonic bandgap for SAR and MIMO systems," *IET Microw., Antennas Propag.*, vol. 14, no. 3, pp. 183–188, Feb. 2020.
- [26] F. Liu, J. Guo, L. Zhao, X. Shen, and Y. Yin, "A meta-surface decoupling method for two linear polarized antenna array in Sub-6 GHz base station applications," *IEEE Access*, vol. 7, pp. 2759–2768, 2019.
- [27] K.-L. Wu, C. Wei, X. Mei, and Z.-Y. Zhang, "Array-antenna decoupling surface," *IEEE Trans. Antennas Propag.*, vol. 65, no. 12, pp. 6728–6738, Dec. 2017.
- [28] J. Li, S. Yang, Y. Gou, J. Hu, and Z. Nie, "Wideband dual-polarized magnetically coupled patch antenna array with high port isolation," *IEEE Trans. Antennas Propag.*, vol. 64, no. 1, pp. 117–125, Jan. 2016.
- [29] Q. Wu, P. Liang, and X. Chen, "A broadband  $\pm 45^\circ$  dual-polarized multiple-input multiple-output antenna for 5G base stations with extra decoupling elements," *J. Commun. Inf. Netw.*, vol. 3, no. 1, pp. 31–37, Mar. 2018.
- [30] Z. Bao, Z. Nie, and X. Zong, "A novel broadband dual-polarization antenna utilizing strong mutual coupling," *IEEE Trans. Antennas Propag.*, vol. 62, no. 1, pp. 450–454, Jan. 2014.
- [31] Y. Cui, R. Li, and H. Fu, "A broadband dual-polarized planar antenna for 2G/3G/LTE base stations," *IEEE Trans. Antennas Propag.*, vol. 62, no. 9, pp. 4836–4840, Sep. 2014.
- [32] Q. Chu, D. Wen, and Y. Luo, "A broadband  $\pm 45^\circ$  dual-polarized antenna with Y-shaped feeding structure," *IEEE Trans. Antennas Propag.*, vol. 63, no. 2, pp. 483–490, Feb. 2015.
- [33] H. Huang, Y. Liu, and S. Gong, "A broadband dual-polarized base station antenna with anti-interference capability," *IEEE Antennas Wireless Propag. Lett.*, vol. 16, pp. 613–616, 2017.
- [34] Y. Luo, Q. Chu, and D. Wen, "A plus/minus 45 degree dual-polarized base-station antenna with enhanced cross-polarization discrimination via addition of four parasitic elements placed in a square contour," *IEEE Trans. Antennas Propag.*, vol. 64, no. 4, pp. 1514–1519, Apr. 2016.





**YUFENG ZHU** was born in Chengdu, Sichuan, China, in 1993. He received the B.Sc. degree in electromagnetics and wireless technology from the University of Electronic Science and Technology of China (UESTC), Chengdu, in 2016, where he is currently pursuing the Ph.D. degree in electromagnetics and microwave technology.

His current research interests include applications of characteristic modes, base station antenna design, and optimization method in antenna design.



**YIKAI CHEN** (Senior Member, IEEE) was born in Hangzhou, China, in 1984. He received the B.Eng. and Ph.D. degrees in electromagnetics and microwave technology from the University of Electronic Science and Technology of China (UESTC), Chengdu, China, in 2006 and 2011, respectively.

From 2011 to 2015, he was a Research Scientist with the Temasek Laboratories, National University of Singapore, Singapore. In 2015, he joined

UESTC, as a Full Professor. He has authored or coauthored over 140 peer-reviewed articles and 34 patents/patent disclosures. He has coauthored the book entitled *Characteristic Modes: Theory and Applications in Antenna Engineering* (John Wiley, 2015) and one book chapter to *Differential Evolution: Fundamentals and Applications in Electrical Engineering* (IEEE Wiley, 2009). His current research interests include antenna engineering, computational electromagnetics, and evolutionary optimization algorithms in electromagnetic engineering.

Dr. Chen is a member of the Applied Computational Electromagnetics Society (ACES). He was a recipient of the National Excellent Doctoral Dissertation Award of China, in 2013. He was recognized as a Hundred Talents Program Professor of the UESTC, a Thousand Talents Program Professor of China, and a Thousand Talents Program Professor of Sichuan Province, China, in 2015, 2016, and 2017, respectively. He has also served on many international conferences as a TPC Member, a Session Organizer, and the Session Chair. He serves as an Associate Editor for *Electronics Letters* and the *Chinese Journal of Electronics* and the review boards of 11 journals.



**SHIWEN YANG** (Fellow, IEEE) was born in Langzhong, Sichuan, China, in 1967. He received the B.S. degree in electronic science and technology from East China Normal University, Shanghai, China, in 1989, and the M.S. degree in electromagnetics and microwave technology and the Ph.D. degree in physical electronics from the University of Electronic Science and Technology of China (UESTC), Chengdu, China, in 1992 and 1998, respectively.

From 1994 to 1998, he was a Lecturer with the Institute of High Energy Electronics, UESTC. From 1998 to 2001, he was a Research Fellow with the School of Electrical and Electronic Engineering, Nanyang Technological University, Singapore. From 2002 to 2005, he was a Research Scientist with Temasek Laboratories, National University of Singapore, Singapore. Since 2005, he has been a Full Professor with the School of Electronic Engineering, UESTC. Since 2015, he has been a Chang-Jiang Professor nominated by the Ministry of Education of China. He has authored or coauthored over 300 technical articles. His current research interests include antennas, antenna arrays, optimization techniques, and computational electromagnetics.

Dr. Yang was a recipient of the Foundation for China Distinguished Young Investigator presented by the National Natural Science Foundation of China, in 2011. He is also the Chair of the IEEE Chengdu AP/EMC Joint Chapter. He serves as an Editorial Board Member for the *International Journal of Antennas and Propagation* and the *Chinese Journal of Electronics*.

• • •